Water Research 289 (2026) 124785

Contents lists available at ScienceDirect

Water Research

journal homepage: www.elsevier.com/locate/watres

Boosting enhanced capacitive deionization of H_2TiO_3/carbon electrodes by yolk-shell construction

Shijun Miao [a,1], Pengcheng Yin [a,1], Shu Zhang [a,1], Zijie Zhang [b], Dawei Li [a], Feihu Li [a,b,*]

[a] Collaborative Innovation Center of Atmospheric Environment and Equipment Technology, Jiangsu Key Laboratory of Atmospheric Environment Monitoring and Pollution Control, School of Environmental Science and Engineering, Nanjing University of Information Science and Technology, 219 Ningliu Road, Nanjing 210044, China

[b] NUIST Reading Academy, Nanjing University of Information Science and Technology, 219 Ningliu Road, Nanjing 210044, China

HIGHLIGHTS

- Yolk-shell HTO/carbon electrodes boost CDI performance with enhanced charge transfer.
- ys-HTO@C achieves 53.1 mg/g Na^+ adsorption and 70.5 % cycling stability.
- HTO/carbon electrodes show Li^+ preference, with a 60.7 Li^+/Na^+ separation factor.
- Capacity fading linked to carbon oxidation and HTO degradation.
- Yolk-shell construction offers potential for better desalination and Li^+ extraction.

GRAPHICAL ABSTRACT

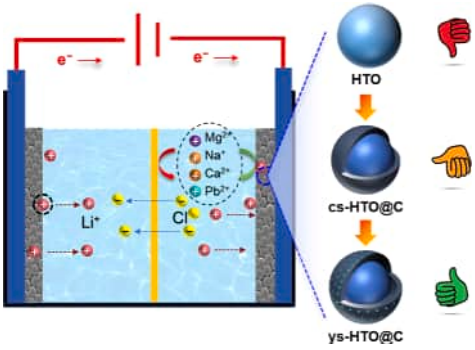

ARTICLE INFO

Keywords:
Metatitanic acid
Rocking-chair capacitive deionization (RCDI)
Desalination
Lithium extraction

ABSTRACT

Capacitive deionization (CDI) is a highly efficient approach for sustainable water desalination and ion-selective separation from complex brines. Layered metatitanic acid (H_2TiO_3, HTO) is a promising platform for electrochemical separation of monovalent ions due to its unique structural properties, but it faces lower conductivity when applied solely to CDI. Coupling HTO with carbon offers a valid strategy to address its charge transfer limitation and thereby enhance the CDI performance. Herein, we report a yolk-shell structured HTO/carbon electrode (denoted as ys-HTO@C) based on a stepwise nanoscale architectonic strategy that demonstrates superior charge transfer and storage properties and, therefore, better CDI performance relative to its core-shell structured and bulk counterparts (denoted as cs-HTO@C and HTO, respectively). Electrochemical desalination reveals that ys-HTO@C electrode has a Na^+ adsorption capacity of 53.1 mg g^{-1} in 500 mg L^{-1} of NaCl solution at 1.2 V, a charge efficiency of 0.68, and moderate cycling stability (70.5 % of capacity retention over 40 cycles) due to its unique void space inside. Structural analyses indicate that capacity fading during cycling is primarily attributed to carbon oxidation and HTO degradation over time. Additionally, lithium extractions in synthetic and actual brines show that the HTO/carbon electrodes exhibit preferential capture of Li^+ over Na^+, Ca^{2+}, Mg^{2+}, and Pb^{2+} ions, with a separation factor of Li^+/Na^+ up to 60.7 for the ys-HTO@C electrodes in natural brine from East

* Corresponding author.
E-mail address: fhli@nuist.edu.cn (F. Li).
[1] These authors contributed equally.

https://doi.org/10.1016/j.watres.2025.124785
Received 25 August 2025; Received in revised form 2 October 2025; Accepted 11 October 2025
Available online 11 October 2025

Taijinaier Salt Lake. It was observed that Li^+ selectivity is concentration-dependent and likely driven by both the HTO's intrinsic Li^+ preference and the ion's properties. The findings underscore the potential of the yolk-shell construction strategy for preparing novel and highly efficient electrodes for electrochemical desalination and selective Li^+ extraction from complex brines.

1. Introduction

Water scarcity has emerged as one of the most pressing global challenges of the 21st century, threatening the health, economic stability, and sustainable development of societies worldwide (Elimelech and Phillip, 2011). According to the United Nations, over 2.2 billion people currently lack access to safely managed drinking water services, and this number is projected to increase with the rapid growth of population, urbanization, and industrialization. Conventional desalination technologies, such as reverse osmosis (RO) and thermal distillation, have been widely adopted to mitigate freshwater shortages. However, these methods suffer from high energy consumption (e.g., ~ 4 kWh m^{-3} of energy is required for 1 m^3 of produced water in the state-of-the-art seawater RO plants), significant operational costs, and environmental concerns related to brine disposal (Elimelech and Phillip, 2011; Suss et al., 2015). As global demand for freshwater accelerates, there is an urgent need for innovative, sustainable, and efficient desalination technologies capable of mitigating water scarcity. Alternatively, electrochemical desalination has emerged as a promising solution due to its energy efficiency, scalability, and potential for integration with renewable energy sources (Wang et al., 2019a). Among various electrochemical techniques, capacitive deionization (CDI) stands out for its low energy demand, environmental friendliness, and ability to operate under mild conditions (Guo et al., 2024; Liu et al., 2024; Oren, 2008). CDI relies on the electrosorption of ions onto porous electrodes, offering a sustainable pathway for brackish water desalination and selective ion removal (Oren, 2008; Porada et al., 2013; Suss et al., 2015). Beyond freshwater production, CDI also offers unique opportunities for the recovery of critical metals from brine streams, such as lithium (Li^+) (Kong et al., 2025; Shang et al., 2022; Yu et al., 2025; Zhou et al., 2025), which has become an essential element for next-generation batteries and renewable energy storage systems (Gamaethiralalage et al., 2021; Mousset et al., 2023; Srimuk et al., 2020). Despite these advantages, the performance of CDI systems heavily depends on the electrode materials, necessitating the development of advanced electrode architectures with high capacitance, excellent conductivity, and long-term stability (Srimuk et al., 2020).

Generally, CDI operates on the principle of electrostatic ion adsorption when an electric field is applied between two oppositely charged electrodes, typically made of porous carbon materials (Oren, 2008; Porada et al., 2012). However, carbon-based electrodes often suffer from poor selectivity, co-ion expulsion, and oxidation-induced degradation, limiting their practical applicability (Gao et al., 2015; Jin et al., 2020; Srimuk et al., 2017). To tackle these challenges, Faradaic electrode materials, particularly metal (hydr)oxides, have been explored due to their redox-active properties and ion-intercalation mechanisms (Srimuk et al., 2020). Of these, titanium-based materials, such as layered metatitanic acid (H_2TiO_3, HTO), have gained considerable attention owing to their unique properties, including low toxicity, layered structure, exchangeable protons, and tunable electrochemical properties (Chitrakar et al., 2014; Li et al., 2023; Ren et al., 2025; Sun et al., 2023; Wei et al., 2020; Xu et al., 2025; Yu et al., 2025; Zhang et al., 2023a). For instance, HTO-based electrodes have demonstrated remarkable sodium (Na^+) and Li^+ adsorption capacities due to their layered structure, which facilitates efficient ion insertion/extraction (Marthi et al., 2021; Zhai et al., 2019). Recent studies have further highlighted the potential of HTO in CDI systems (Orooji et al., 2022; Yang et al., 2024; Yu et al., 2025), where its synergistic combination with carbon materials enhances charge transfer kinetics while maintaining structural integrity (Zhang et al., 2023b). Despite these advances, the practical deployment of HTO electrodes is still limited by poor capacity and slow kinetics (Sun et al., 2024), calling for innovative structural engineering strategies to optimize their performance.

To improve the desalination performance of CDI electrodes, several strategies have been employed, including heteroatom doping, surface functionalization, and nanoscale architectonics (Bao et al., 2023; Ma et al., 2025; Srimuk et al., 2020). Recently, rational design of nanostructured electrode architectures—such as core-shell, yolk-shell, and other hierarchical structures—has opened new avenues for optimizing electrochemical performance (Liu et al., 2023; Zhang et al., 2025). Core-shell and yolk-shell nanostructures have emerged as particularly promising due to their unique properties, such as high surface area, optimized mass transport, and alleviated volume expansion during ion intercalation (Liu et al., 2023). The yolk-shell configuration, characterized by a movable core within a hollow shell, offers distinct advantages, including buffered internal space for volume changes and shortened ion diffusion pathways (Liu et al., 2023; Zhang et al., 2025). To date, yolk-shell structured HTO electrodes and their potential in CDI remain underexplored, and the relationship between the yolk-shell structure and its electrochemical performance has yet to be explored. Given the inherent advantages of HTO and the structural benefits of yolk-shell designs, combining these aspects could significantly improve CDI performance, warranting systematic investigation.

This work aims to design and evaluate yolk-shell structured HTO/carbon electrodes for high-performance CDI by systematically comparing their desalination efficiency with bulk and core-shell structured HTO/carbon counterparts. Specifically, we prepared three distinct HTO morphologies—bulk, core-shell, and yolk-shell—through nanoscale architectonic processes. The yolk-shell HTO/carbon electrode is expected to exhibit superior desalination capacity, cycling stability, and capability retention due to its unique structure, which facilitates rapid ion diffusion and accommodates volume changes during cycling. Furthermore, given the intrinsic Li^+ preference of HTO, we also evaluated the Li^+ extraction performance of the HTO/carbon electrodes in synthetic and natural brines. This study provides fundamental insights into the structure-performance relationship of HTO-based CDI electrodes, guiding future material design for electrochemical desalination and Li^+ extraction. Beyond CDI, the proposed yolk-shell construction strategy could be extended to other energy storage materials.

2. Experimental section

All chemicals are of analytical grade or above and used without further purification. Ultrapure deionized water (DI H_2O, 18.2 MΩ·cm at 25 °C) was used for preparing all solutions in this study.

2.1. Synthesis of yolk-shell structured ys-HTO@C

As depicted in Fig. 1a, the yolk-shell structured HTO/carbon was facilely prepared using a stepwise nanoscale architectonics procedure. Briefly, 5.0 g of TiO_2 powder (≥99.0 %, Aladdin Chemical Inc.) and 4.633 g of NaCl powder (99.5 %, Macklin Inc.) were placed in a mortar and milled manually for 30 min using a small amount of ethanol as the medium. Then, the obtained homogenous mixture was heated in a muffle furnace to 700 °C at a rate of 6 °C/min and maintained for 4 h to obtain $Na_3Ti_{0.25}O_2$ (denoted as NTO). A certain amount of the as-prepared NTO was then transferred to a beaker with 100 mL of 0.2 mol L^{-1} HCl solution to achieve a solid-liquid ratio of 2 g L^{-1}, followed

by stirring continuously at 60 rpm in a water bath (*ca.* 60 °C) for 12 h to fully exchange sodium with hydrogen ions (H^+). The precipitate was separated centrifugally, washed with excessive DI H_2O and ethanol (EtOH), and dried at 60 °C in a vacuum oven overnight to obtain HTO.

Subsequently, 60 mg of the as-prepared HTO was added to a mixture of 140 mL of EtOH, 20 mL of DI H_2O, and 6 mL of $NH_3{\cdot}H_2O$ (≥ 28 %, Aladdin Chemical Inc.), followed by magnetically stirring (60~80 rpm) at room temperature for 15 min. Then, 1 mL of tetrapropyl orthosilicate (TPOS, ≥ 97 %, Aladdin Chemical Inc.) was added and stirred for 15 min to coat the as-prepared HTO particulates with a SiO_2 shell. Next, 0.2 g of $C_6H_6O_2$ (≥99 %, Macklin Inc.) and 0.28 mL of CH_2O (37–40 %, Sinopharm Chemical Inc.) were added to the above suspension, following by gently stirring (60~80 rpm) at room temperature for 24 h to allow the condensation of resorcinol formaldehyde (RF) over the surface of SiO_2-coated HTO, yielding the core-shell-shell structured composite. The composite was then separated by centrifugation, washed with excessive DI H_2O and EtOH, and dried in a vacuum oven (*ca.* 60 °C) overnight (denoted by css-HTO/SiO_2/RF).

Next, the obtained css-HTO/SiO_2/RF was heated in a muffle furnace under a nitrogen (N_2) atmosphere to 700 °C (2 °C/min) and maintained for 5 h to obtain the core-shell-shell structured composite (i.e., css-HTO/SiO_2/C). The as-prepared css-HTO/SiO_2/C was chemically etched in a 4 M NaOH solution (*ca.* 60 °C) for 4 h to remove the intercalated SiO_2 shell. Then, precipitate was collected centrifugally, washed repeatedly with DI H_2O and EtOH, and dried overnight in a vacuum oven at 60 °C to obtain the yolk-shell structured HTO/carbon (denoted by ys-HTO@C). For comparison, core-shell structured HTO/carbon was also prepared (Text S1, Supporting Information).

2.2. Characterizations

The morphology, crystallography, surface functional groups, and elemental composition of the as-prepared HTO/carbon composites were examined comprehensively. Explicitly, the microscopic morphology of the as-prepared HTO/carbon composites was inspected on a ZEISS Gemini 300 field emission scanning electron microscope (SEM, ZEISS, Germany), along with a Philips TECNAI 12 transmission electron microscope (TEM), respectively. The particle size was examined by Nano Measurer (ver. 1.2.0) based on SEM images. Energy dispersive X-ray spectroscopy (EDX) was employed to collect the elemental mapping data of the samples. X-ray diffraction (XRD) analysis was performed on an XRD-6100 diffractometer (XRD, Shimadzu, Japan) at a tube voltage of

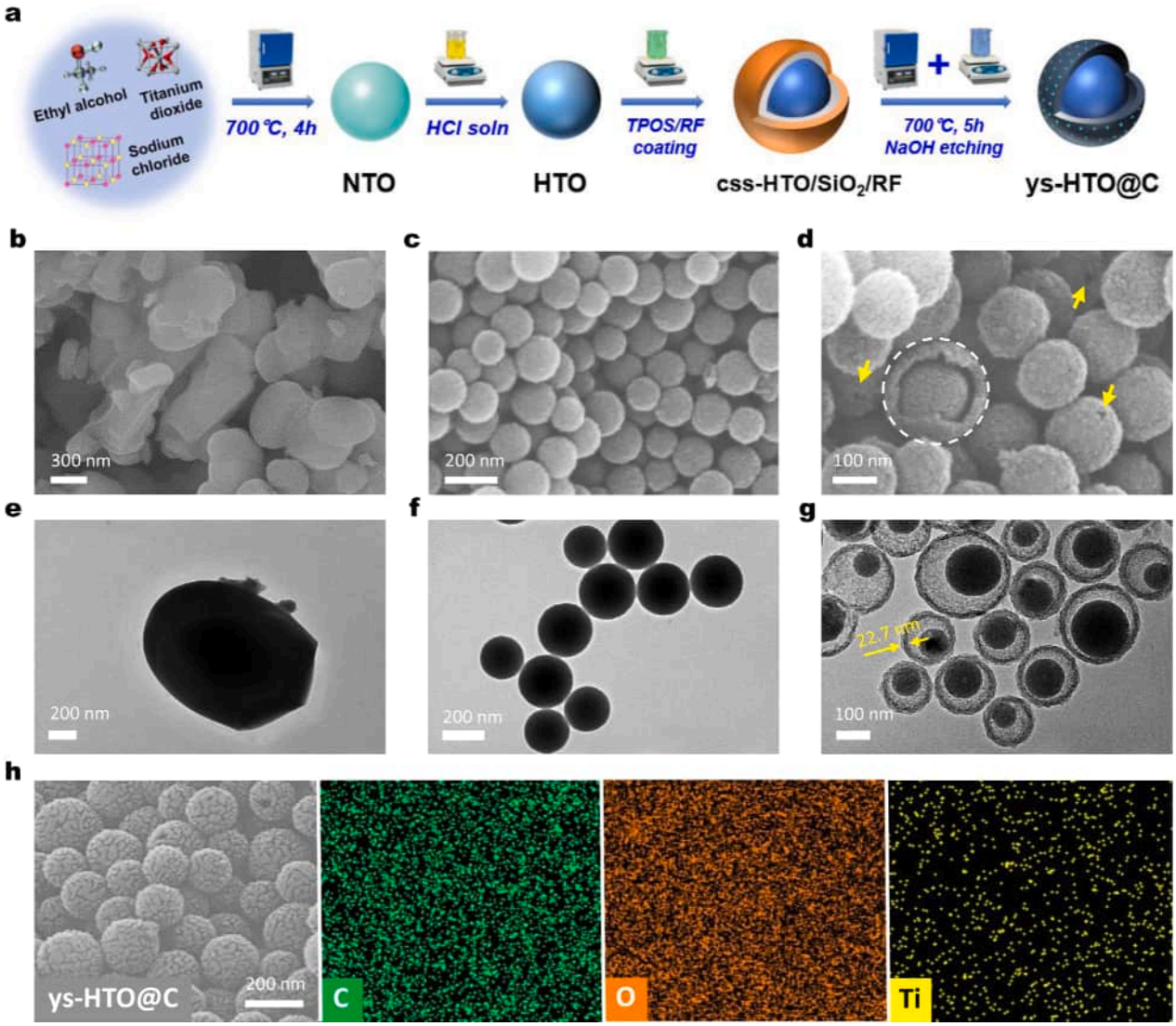

Fig. 1. (**a**) Schematic illustration of the preparation of ys-HTO@C; (**b-d**) SEM images of the as-prepared (**b**) HTO, (**c**) cs-HTO@C, and (**d**) ys-HTO@C; (**e-g**) TEM images of the as-prepared (**e**) HTO, (**f**) cs-HTO@C, and (**g**) ys-HTO@C; (**h**) SEM image and the corresponding EDX mapping of ys-HTO@C. Note in panel **d**, the white dotted circle verifies the yolk-shell structure, while the yellow arrows indicate the porous channels within the carbon shells.

40 kV and a tube current of 30 mA with Cu-Kα radiation. X-ray photoelectron spectroscopy (XPS) was conducted on an electron spectrometer (UIVAC-PHI, Japan) using 300 W Al Kα radiation, with the adventitious carbon species C 1 s (284.8 eV) for binding energy (BE) correction. Fourier transform infrared (FTIR) spectrum measurement was carried out on an infrared spectrometer (Nicolet iS5, Thermo Fisher, USA) using the KBr method.

2.3. Electrochemical measurements

All electrochemical measurements were performed in a 1.0 M NaCl solution using a Correst CS310H electrochemical workstation (Correst Instruments Inc., China) with a three-electrode system: a platinum sheet electrode as the counter electrode, Ag/AgCl as the reference electrode, and the electrode containing HTO/carbon as the working electrode. The working electrode was prepared as follows: i) HTO/carbon, acetylene black (Alfa Aesar, China), and polyvinylidene fluoride (PVDF, Aladdin Chemical Inc.) were mixed in a mass ratio of 8:1:1; ii) the mixture was dispersed and milled manually with 1-methyl-2-pyrrolidone (NMP, ≥99.5 %, Macklin Inc.) until a uniform slurry was obtained; iii) the slurry was then dropped onto a 1 cm × 1 cm clean graphite paper and dried at 80 °C in a vacuum oven for 2 h to obtain the working electrode. Cyclic voltammetry (CV) was performed at scan rates of 5, 10, 20, 50, and 100 mV s^{-1} within a potential window of 0 to 1.0 V, galvanostatic charge-discharge (GCD) analysis was conducted at current densities of 0.3, 0.4, 0.5, 1.0, 2.0, 3.0, 4.0, and 5.0 A g^{-1}, and electrochemical impedance spectroscopy (EIS) measurements were carried out in the frequency range of 10^5 to 0.01 Hz with a bias voltage and ac amplitude being set at open-circuit and 5 mV, respectively. The details of electrochemical measurements are provided in Text S2.

2.4. Capacitive deionization experiments

The electrodes for CDI testing were prepared following the same protocol described in our earlier works (Bao et al., 2023; Zhang et al., 2025). After preparation, the electrodes to be tested were assembled into the desalination cell (Fig. S1a, Supporting Information) and subsequently mounted on the RCDI desalination platform (Fig. S1b). Following the same procedure described elsewhere (Zhang et al., 2025), the desalination test was performed in batch mode under a constant voltage, with short-circuiting as the desorption operation. Conventionally, voltages of 0.6−1.2 V and feed brines of 100−500 ppm of NaCl were employed to evaluate the impacts of cell voltage and feed brines on the desalination performance, respectively, with the following metrics: salt adsorption capacity (**Γ**), salt adsorption rate (***SAR***), charge efficiency (**Λ**), cycling performance and energy consumption. More details on the desalination operations and calculations are given in Text S3. To examine the ion preference of these HTO/carbon electrodes toward specific ions, ion-selective adsorption tests were performed in both the synthetic brine (Li^+:Na^+:K^+:Mg^{2+}:Ca^{2+} = 4:79:16:18:5, molar ratio) and the diluted brine from the East Taijinaier Salt Lake (Table S1) following the same protocol described earlier (Bao et al., 2022). The operations of ion selectivity tests are detailed in Text S4.

3. Results and discussion

3.1. Characteristics of the as-prepared HTO/carbon materials

The morphological features of the HTO/carbon composites are depicted in Fig. 1b-h. The as-prepared HTO exhibits a near-oval morphology (Fig. 1b), consistent with previous reports on hydrated titanate nanostructures (Chitrakar et al., 2014; Wang et al., 2019a). However, upon coating with SiO_2 and/or carbon (Fig. 1a), the morphology transitioned into uniform spherical particles, as observed in both cs-HTO@C (Fig. 1c) and ys-HTO@C (Fig. 1d), with mean diameters of 150 and 168 nm, respectively. This morphological transformation may be attributed to a twofold mechanism: i) chemical etching-recrystallization during the SiO_2 coating process, which promotes structural rearrangement (Hagemans et al., 2017), and ii) conformal carbon deposition, which smoothens the surface and reduces anisotropic growth tendencies (Aramesh et al., 2017). The yolk-shell (ys-HTO@C) architecture is particularly evident in Fig. 1d, where a distinct contrast between the yolk and the hollow carbon shell is highlighted by the dashed-line circle. This structural feature is advantageous for ion-storage applications, as the void space accommodates volume expansion during cycling, mitigating mechanical degradation (Liu et al., 2023). TEM analysis (Fig. 1e-g) further confirms the morphology of these HTO/carbon observed in SEM (Fig. 1b-d), with ys-HTO@C displaying a well-defined carbon shell with a mean thickness of 22.7 ± 0.2 nm (Figs. 1g, and S2a), ensuring structural integrity and enhanced electronic conductivity. Additionally, EDX elemental mapping (Fig. 1h) reveals a homogeneous distribution of C, O, and Ti, with carbon being the most abundant, as expected for the carbon-coated ys-HTO@C. The uniform dispersion of these elements supports the successful formation of a yolk-shell architecture, crucial for optimizing electrochemical performance.

Structurally, layered HTO crystallizes in a framework analogous to layered titanates, comprising edge- and corner-sharing TiO_6 octahedral layers intercalated with protons (H^+), often as structural water or hydroxyl groups (Fig. 2a). This structural arrangement facilitates cation exchange and intercalation, making HTO a promising candidate for energy storage and ion-exchange applications (Chitrakar et al., 2014; Zhang et al., 2023b). XRD analysis (Fig. 2b) confirms the successful synthesis of HTO, with patterns basically matching the standard Li_2TiO_3 phase (JCPDS #33–0831), indicating a crystallized structure (Chitrakar et al., 2014). The broad diffuse hump over a 2θ range of 15−30 in the HTO (black curve) appears to be attributed to the amorphous phases. Notably, both cs-HTO@C and ys-HTO@C exhibit a broad diffuse hump spanning the 2θ range of 15–30°, characteristic of amorphous carbon coatings, which is consistent with previous studies on carbon-encapsulated metal oxides (Liu et al., 2023, 2019). This amorphous carbon phase contributes to enhanced electronic conductivity, a critical factor for electrode materials in batteries and supercapacitors. Further chemical bonding characteristics were probed using Fourier-transform infrared (FTIR) spectroscopy. The FTIR spectra (Fig. 2c) of pristine HTO are marked by typical stretching (3432 and 3203 cm^{-1}) and bending (1624 and 1380 cm^{-1}) vibrations corresponding to –OH groups of water—either adsorbed or structural—as well as a dominant broad absorption in the 400–800 cm^{-1} region assignable to Ti–O lattice vibrations (Chitrakar et al., 2014; Tian et al., 2023). Upon carbon encapsulation, the carbon-coated composites (cs-HTO@C and ys-HTO@C) exhibit additional IR bands at 1118 cm^{-1} (C–O stretching), confirming the presence of carbonaceous functional groups (Smith, 2022). The persistence of the Ti–O characteristic at 472 cm^{-1} and 798 cm^{-1} (Ti–O–Ti bending) in the composites indicates retention of the HTO framework despite surface modification (Bandina et al., 2025). Notably, coating with carbon shell appears to slightly improve the hydrophilicity of the as-prepared HTO/carbon, as evidenced by the changes in the C═O (at 1720 cm^{-1}) stretches (inset in Fig. 2c), thereby favoring the initial ion adsorption kinetics. XPS analysis (Fig. 2d-f) further corroborates the presence of C, O, and Ti within the composites, and critically, deconvolution of the Ti 2p spectrum yields a spin-orbit splitting (ΔE ≈ 5.7 eV) consistent with Ti(IV) oxidation state, thereby confirming the preservation of the chemical environment of titanium atoms across all composites. Note that both the as-prepared ys-HTO@C and cs-HTO@C demonstrated high sp^2/sp^3 ratios (i.e., 0.84 and 0.89) as evidenced in the C 1s regional XPS spectra (Fig. S2b), endowing their high conductivity when applied to CDI. These findings collectively demonstrate the successful integration of carbon coatings while preserving the structural integrity of HTO, thus rendering them structurally robust and chemically versatile.

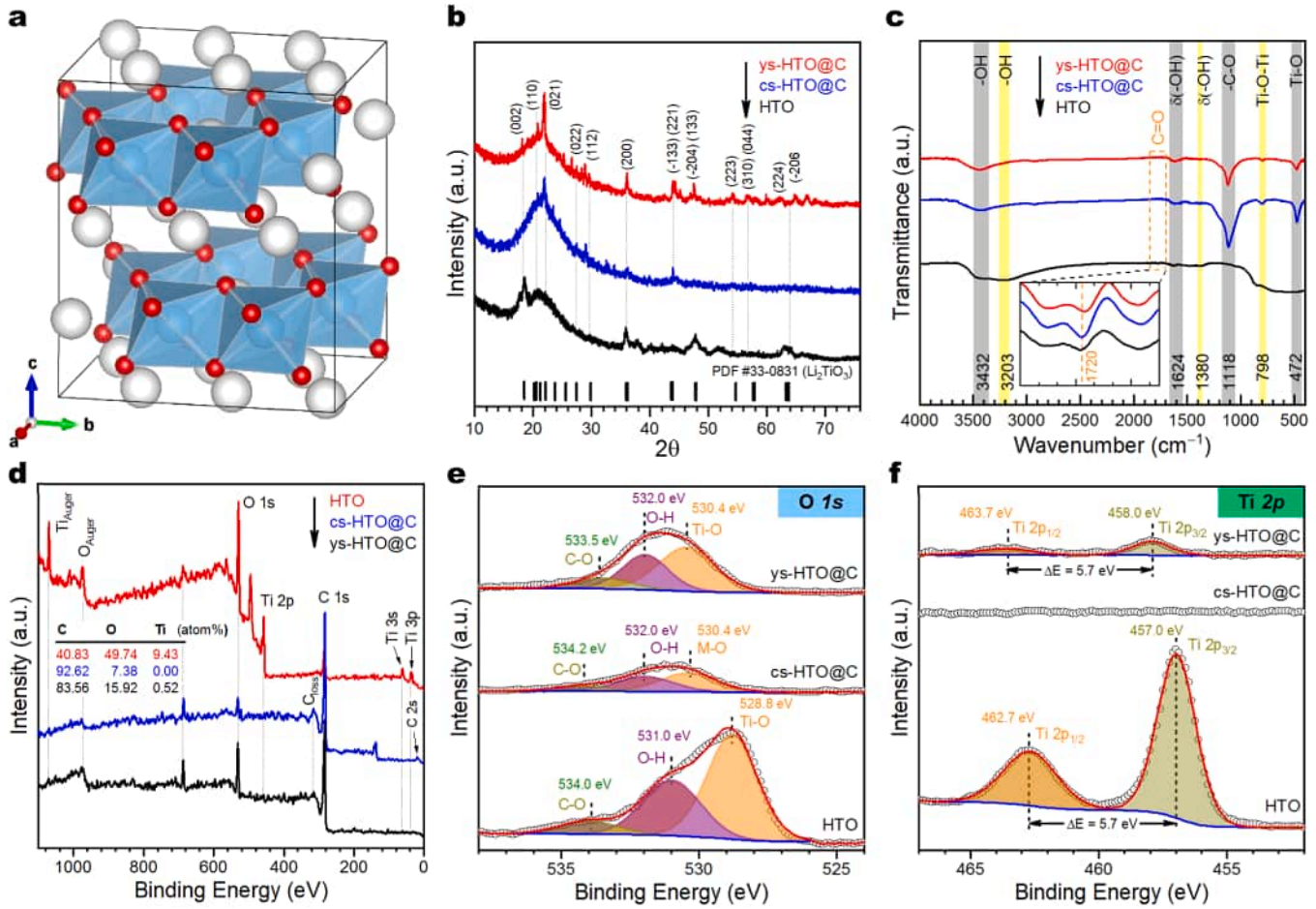

Fig. 2. (**a**) Crystal structure of the layered H_2TiO_3 (HTO) with the while, cyan, and red balls corresponding to H, Ti, and O atoms, respectively (created by VESTA); (**b**) XRD patterns, (**c**) FTIR, (**d**-**f**) XPS spectra of the as-prepared HTO, cs-HTO@C, and ys-HTO@C: (**d**) survey XPS spectra, (**e**) O 1*s* , and (**f**) Ti 2*d* regions.

3.2. Electrochemical properties of HTO/carbon electrodes

The electrochemical characteristics of the three HTO/carbon electrodes—ys-HTO@C (yolk-shell), cs-HTO@C (core-shell), and pristine HTO—were systematically evaluated using cyclic voltammetry (CV), galvanostatic charge-discharge (GCD), and electrochemical impedance spectroscopy (EIS) in 1 M NaCl solution. The CV curves of these electrodes are depicted in Fig. S3. As the scan rate was increased from 5 to 100 mV s^{-1}, all HTO/carbon electrodes exhibited a notable distortion in their voltammogram profiles, culminating in a distinctly leaflike shape at the highest scan rate. This characteristic behavior is indicative of pseudocapacitive charge storage commonly associated with Faradaic electrodes dominated by ion insertion or surface redox processes—the so-called capacitor-like Faradaic electrodes (Srimuk et al., 2020; Wang et al., 2019b) rather than carbon-based electrodes interfered by polarization, particularly at higher scan rates (Wang et al., 2014). Notably, the integrated CV area at 5 mV s^{-1} (Fig. 3a) followed the order ys-HTO@C > cs-HTO@C > HTO, reflecting the superior charge storage capacity of ys-HTO@C relative to the other electrodes, given the direct proportionality between CV area and stored charge. Further deconvolution of charge storage mechanisms (Fig. 3b,c) revealed contributions from capacitive (surface-mediated) and diffusion-controlled (bulk insertion) processes (Wang et al., 2007). The total charge storage in these electrodes arises from three components: (i) diffusion-controlled Na^+ insertion, (ii) pseudocapacitive charge transfer with surface and interlayer Ti atoms, and (iii) non-Faradaic electric double-layer capacitance (EDL). However, EDL contributions typically account for <10 % of total capacitance in metal oxide electrodes (Brezesinski et al., 2010), suggesting that pseudocapacitive mechanisms dominate in these HTO/carbon composites. Specifically, the reversible redox process ($H_2TiO_3 + 2Na^+ + 2e^- \leftrightarrow Na_2TiO_3 + 2H^+$) at or near the electrode surface is believed to be the principal pseudocapacitive reaction (Li et al., 2005; 2006). Consistently, the quantified pseudocapacitance at 5 mV s^{-1} (see Fig. 3c and supplementary Figs. S4–S6) exhibits the order ys-HTO@C > cs-HTO@C > HTO, supporting the assertion that the charge storage capabilities of these electrodes are directly linked to their pseudocapacitive performance.

Complementary to the CV results, the GCD measurements (Fig. S7a–c) further corroborated these findings, with all electrodes exhibiting symmetrical triangular curves, indicative of highly reversible charge-discharge behavior in NaCl electrolyte. The iR drops were observed to increase linearly with discharge current within the range of 0–40 mV for these HTO/carbon electrodes (Fig. S7d), with the lowest values in the ys-HTO@C electrode, validating its lowest internal charge-transfer resistances (Jin et al., 2020). Notably, the ys-HTO@C electrode exhibits a substantially longer charge-discharge duration (*cf*. GCD curves at 1 A g^{-1} in Fig. 3d), signifying its enhanced capacitive performance and corroborating the CV findings. Quantitative analysis of the specific capacitance, as derived from the discharge branches of GCD curves (excluding the iR drop, Fig. 3e), reveals a decreasing trend with increasing current density, yet consistently follows the order ys-HTO@C > cs-HTO@C > HTO across all tested scenarios. For instance, these HTO/carbon demonstrated specific capacitances of 506.53, 134.35, and 116.76 F g^{-1} for ys-HTO@C, cs-HTO@C, and HTO at 0.3 A g^{-1}, respectively (Table S2). This further substantiates the superior charge storage capacity of the ys-HTO@C electrode. Additionally, EIS

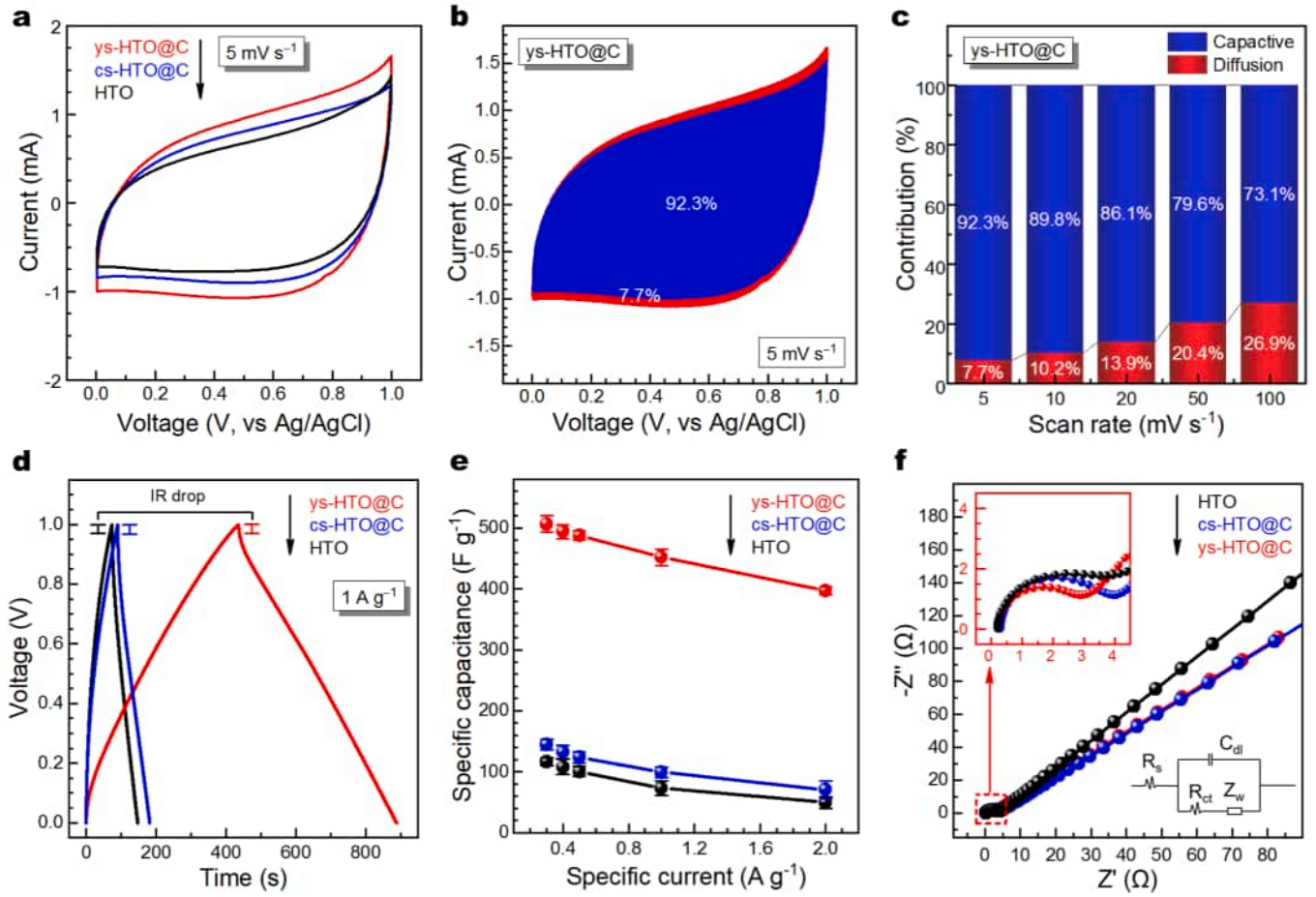

Fig. 3. Electrochemical characterizations of HTO/carbon electrodes: (**a**) CV curves at a scan rate of 5 mV s^{-1} in 1 M NaCl solution; (**b**) Capacitive- and diffusion-controlled contribution to the charge storage of the ys-HTO@C electrode at 5 mV s^{-1}; (**c**) Contribution percentages of capacitive- and diffusion-controlled capacity for the ys-HTO@C electrode at varying scan rates; (**d**) GCD curves at 1 A g^{-1} in 1 M NaCl solution; (**e**) specific capacitance at different current densities; (**f**) Nyquist plots of EIS and the fitting curves, inset at the lower right is the equivalent circuit.

measurements (Fig. 3f, Table S2) show that the charge transfer resistance (R_{ct}) values for ys-HTO@C, cs-HTO@C, and pure HTO are 2.55, 3.29, and 3.44 Ω, respectively, while their equivalent series resistance (R_s) values are marginally low and comparable (0.20, 0.21, and 0.30 Ω). The lowest R_{ct} for ys-HTO@C indicates most facile charge transfer kinetics at the electrode/electrolyte interface, likely promoted by the improved conductivity, yolk-shell hierarchical structure, and tailored surface chemistry of the carbon coating. Furthermore, the slope of the straight lines refers to the Warburg impedance (Z_w), signifying the interfacial ion migration from the electrolyte to the electrodes. Notably, the slope demonstrates a trend of ys-HTO@C ≈ cs-HTO@C < HTO, indicating a higher interfacial ion transfer rate in both the ys-HTO@C and cs-HTO@C than the bulk HTO electrode (Table S2). Collectively, these results demonstrate that ys-HTO@C exhibits the most favorable electrochemical properties among the tested electrodes, including optimal charge storage kinetics, minimal charge transfer resistance, and exceptional pseudocapacitance, thereby positioning it as the prime candidate for CDI applications.

3.3. Capacitive deionization performance

To systematically evaluate the electrochemical desalination performance of the HTO/carbon electrodes, batch mode experiments were performed on a rocking-chair capacitive deionization (RCDI) platform. In a typical charging-discharging cycle (corresponding to adsorption-desorption) using a 100 mg L^{-1} (1.71 mM) NaCl solution at 1.2 V, all electrodes exhibited an immediate and significant decline in solution conductivity, rapidly approaching a plateau as ion adsorption proceeded, followed by swift recovery of conductivity to near-initial levels upon electric discharge (Fig. 4a). This pronounced reversibility in conductivity change underscores the excellent electrochemical reversibility of all HTO/carbon electrodes, which is consistent with their GCD profiles (Fig. 3d).

The calculated salt adsorption capacities (**Γ**) for these electrodes demonstrate a clear hierarchy: 48.7 mg g^{-1} for ys-HTO@C, 17.6 mg g^{-1} for cs-HTO@C, and 11.6 mg g^{-1} for pristine HTO (Fig. S8a). This result confirms the superior Na^+ storage capability of the ys-HTO@C electrode, which can be attributed to the distinct void space enabled by its yolk-shell architecture, effectively facilitating cation storage (Liu et al., 2023). In line with this, current response curves and charge efficiency (**Λ**) analyses (Fig. 4b) further differentiate the three electrodes, with **Λ** values of 0.68 for ys-HTO@C, 0.59 for cs-HTO@C, and 0.52 for HTO, respectively. Such results highlight the remarkable charge utilization efficiency of the yolk-shell structured electrode relative to the others, a trend that is further substantiated by the Kim-Yoon plot analyses (Fig. 4c). Specifically, for the ys-HTO@C electrode, the shortest distance to the upper-right corner in the ***SAR*** versus **Γ** plots reveals its ability to trap ions at both the fastest rate and with the highest storage capacity compared to the other electrodes, indicating a synergistic enhancement derived from the yolk-shell configuration.

Further explorations into the influence of operational parameters, including applied cell voltage and feed saline concentration, provide additional insight into the CDI performance of these HTO/carbon electrodes (Figs. 4d, 4e, and S8). Since the driving force for the capacitive

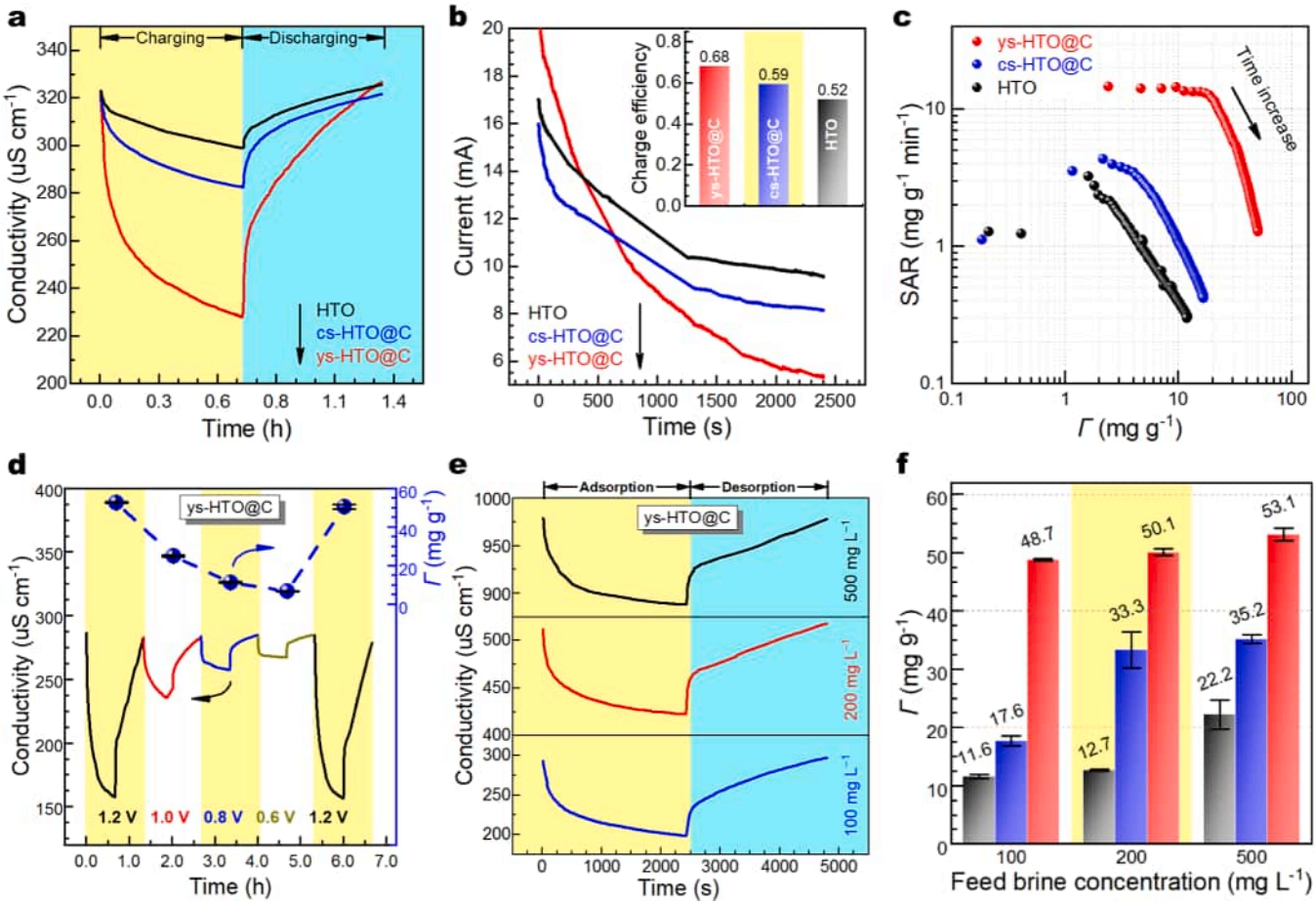

Fig. 4. (**a**) Plots of conductivity versus time in one charge-discharge operation of CDI cell with HTO/carbon electrodes in 100 mg L^{-1} NaCl solution at 1.2 V; (**b**) Current response and the corresponding charge efficiency of these HTO/carbon electrodes; (**c**) Kim-Yoon plots; (**d-e**) Plots of conductivity versus time of CDI cells with the ys-HTO@C electrode (**d**) at varying voltages in 100 NaCl solution and (**e**) in feed brines with varying concentrations at 1.2 V; (**f**) Comparison of the salt adsorption capacity (**Γ**) of these HTO/carbon electrodes in feed brines with varying concentrations at 1.2 V.

deionization process fundamentally stems from the externally applied electric field (Suss et al., 2015), a systematic decrease in cell voltage from 1.2 V to 0.6 V led to concomitant declines in solution conductivity and the relevant **Γ** values, as anticipated (Figs. 4d, and S8). Importantly, upon restoring the cell voltage from 0.6 to 1.2 V, the electrodes regained their original desalination performance, demonstrating the robust reversibility and electrochemical stability (Oren, 2008; Suss et al., 2015). In parallel, the performance of the electrodes was also observed to be dependent on the initial concentration of the saline feed (Figs. 4e, and S8). Higher NaCl concentrations resulted in more rapid adsorption equilibria and greater adsorption capacities, a trend exemplified by the ys-HTO@C electrode, which achieved **Γ** values of 48.7, 50.1, and 53.1 mg g^{-1} in 100, 200, and 500 mg L^{-1} of NaCl solutions, respectively (Fig. 4f). This serial enhancement in salt removal can be rationalized not only by the increased concentration gradient providing an additional driving force for ion migration beyond the electric field (Han et al., 2013)—but also by the improved accessibility of the inside channels to ions at higher concentrations. Notably, among the three electrodes, ys-HTO@C consistently outperformed both cs-HTO@C and pristine HTO across all concentrations (Fig. 4f), firmly reaffirming the structural merits (especially the internal void for ion accommodation and transport) of the yolk-shell design (Gan et al., 2023; Liu et al., 2023; Seo et al., 2023).

Additionally, when compared with other yolk-shell structured electrodes previously applied to CDI (Fig. S8f and Table S3), ys-HTO@C achieves a significantly higher **Γ** under similar conditions, aligning it at the forefront of current CDI electrode materials. This demonstration of consistently superior desalination capacity and efficiency, together with its rapid adsorption kinetics and excellent operational stability, collectively highlights the practical and scalable potential of the ys-HTO@C electrode for practical applications. The integrated results explicitly establish that the yolk-shell architecture of ys-HTO@C imparts a compelling advantage in both capacity and rate capability, thereby offering a promising direction for the development of advanced CDI electrodes.

3.4. *Cycling performance*

The cycling stability of electrode materials stands as a critical criterion for their practical application. To comprehensively evaluate the cycling performance of these HTO/carbon electrodes (i.e., ys-HTO@C, cs-HTO@C, and HTO), repeated cycling tests were conducted in 500 mg L^{-1} NaCl solution at two voltages (i.e., 1.2 V and 0.8 V), given that carbon oxidation—particularly at 1.2 V—is a well-documented contributor to capacity fading during the consecutive charge-discharge operations (Gao et al., 2015; Jin et al., 2020; Srimuk et al., 2017). When initially subjected to 60 continuous charge–discharge cycles in 500 mg L^{-1} NaCl solution at 1.2 V (Fig. S9a-c), all electrodes exhibited high initial **Γ** values in the early cycles (e.g., 0–10 cycles). However, this capacity deteriorated markedly with progressive cycling, resulting in poor **Γ** retention outcomes: specifically, 51.8 % for ys-HTO@C, 50.0 % for cs-HTO@C, and 47.2 % for pristine HTO, respectively (Fig. S9d). The pronounced capacity fading observed at 1.2 V for all electrode types is in good agreement with previous studies and can be primarily attributed to

the irreversible oxidation and subsequent degradation of the carbon shell or matrix within the composite electrodes (Gao et al., 2015; Srimuk et al., 2017). High voltage, while accelerating the kinetics of ion capture and initially enhancing ion storage, thereby fundamentally compromises the structural durability and lifespan of these materials, as evidenced by the pronounced **Γ** retention drop.

To gain further insight into the interplay between operational voltage, cycling stability, and ion adsorption performance, we subsequently performed parallel cycling tests at the reduced voltage of 0.8 V. Interestingly, all electrodes exhibited lower initial **Γ** values relative to their high-voltage counterparts, which is consistent with the expectation that lower driving force limits maximum ionic intercalation or adsorption during each cycle (*cf*. Figs. 5a, b, and S9d). Nevertheless, all electrodes demonstrated significantly improved **Γ** retentions—70.5 % for ys-HTO@C, 66.5 % for cs-HTO@C, and 64.1 % for HTO—thereby signifying a clear trade-off between capacity magnitude and cycling performance. This inverse relationship between operational voltage and cycling stability underscores a critical balance between maximizing ion storage versus maintaining electrode integrity over extended cycling operations: higher voltages maximize initial capacity but compromise longevity of the electrodes, whereas lower voltages extend electrode lifespan at the expense of adsorption capacity (Figs. S9 and S10a,b).

Post-cycling structural characterizations of the ys-HTO@C electrode reveal further insights into degradation mechanisms. XRD and FTIR analyses of the cycled ys-HTO@C electrode confirm not only carbon oxidation but also significant HTO phase deterioration (Fig. 5c, d), consistent with our earlier findings observed in MnO_2 and NiHCF/carbon electrodes (Bao et al., 2023, 2022; Jin et al., 2025, 2020; Zhang et al., 2025). Furthermore, quantitative analysis by ICP-OES shows that the cumulative titanium (Ti) leaching from HTO into the solution followed the trend ys-HTO@C < cs-HTO@C < HTO, with the highest Ti release (0.74 mg L^{-1}) from the uncoated HTO electrode (Fig. S10c). This observation suggests that structural degradation of HTO contributes majorly to the progressive **Γ** loss. The yolk-shell architecture of ys-HTO@C appears to mitigate HTO dissolution to some degree, as its carbon shell likely shields the HTO core from direct electrolyte exposure, thus preserving electrode function more effectively over time. Collectively, these findings demonstrate that ys-HTO@C offers the best compromise between **Γ** retention and durability, highlighting the yolk-shell design's superiority in stabilizing both carbon and HTO components. Specifically, the unique void space within the yolk-shell structure serves a dual function: it not only buffers volumetric expansion and contraction during ion insertion/extraction (thereby reducing mechanical rupture) but also creates additional diffusion paths and limits direct exposure of HTO to the electrolyte, slowing down both physical and chemical degradation processes (Liu et al., 2023). However, the persistent capacity recession across all electrodes—driven by carbon oxidation and HTO degradation—calls for further research into advanced strategies to achieve long-term stability (e.g., over hundreds of cycles) without sacrificing performance for practical applications.

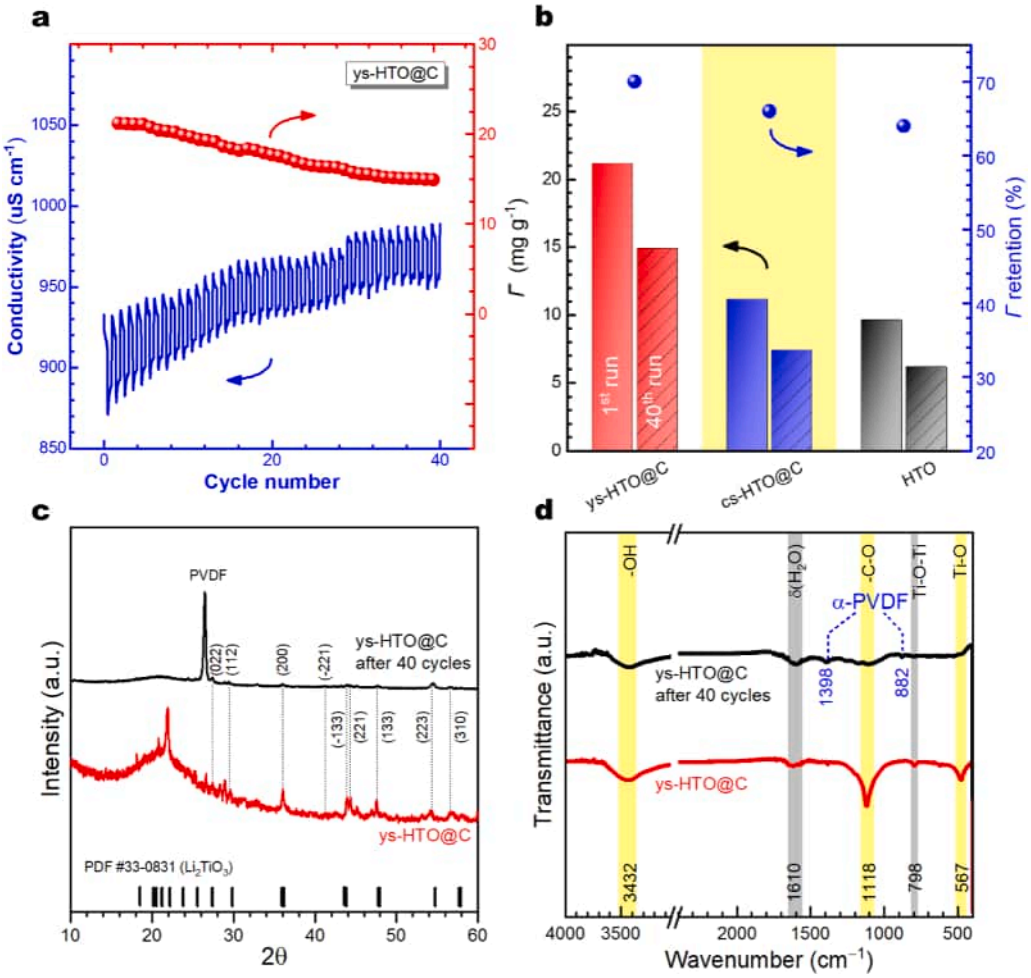

Fig. 5. Cycling performance of HTO/carbon electrodes in 500 ppm NaCl solution at 0.8 V: (**a**) Plots of conductivity and the corresponding **Γ** of ys-HTO@C; (**b**) comparison of **Γ** and **Γ** retention (%) of HTO/carbon electrodes; (**c**) XRD patterns and (**d**) FTIR spectra of the as-prepared ys-HTO@C composite and the ys-HTO@C electrode after the 40th cycle of CDI operations.

3.5. Ion selectivity

The electrochemical characterizations of three HTO/carbon electrodes (HTO, cs-HTO@C, and ys-HTO@C) reveal a pronounced selectivity for lithium ions (Li^+) over competing cations, reflecting HTO's established intrinsic preference for monovalent ions, particularly Li^+ (Chitrakar et al., 2014; Li et al., 2023; Xu et al., 2016; Zhang et al., 2023b). To rigorously evaluate the Li^+ ion selectivity of these electrodes, electrosorption experiments were carried out both in synthetic brine—comprising equimolar cations (10 mM of Li^+, Na^+, Ca^{2+}, Mg^{2+}, and Pb^{2+})—and in actual brine from East Taijinaier Salt Lake (Qinghai, China) mimicking real-world salinities and ion ratios (Table S1). In synthetic brine, the adsorption behavior of each cation as a function of time shows nearly linear increases in concentration variation (ΔC) for all electrodes (Figs. 6a, S11a, and S12a), following a consistent sequence: ΔC (Li^+) > ΔC (Na^+) > ΔC (Ca^{2+}) > ΔC (Mg^{2+}) > ΔC (Pb^{2+}). This trend is also mirrored in the cation adsorption capacity (Γ, mmol g^{-1}), where Γ (Li^+) > Γ (Na^+) > Γ (Ca^{2+}) > Γ (Mg^{2+}) > Γ (Pb^{2+}), confirming the superior affinity of HTO/carbon electrodes toward Li^+ over Na^+, Ca^{2+}, Mg^{2+}, and Pb^{2+} (i.e., the cation affinity of these electrodes follows $Li^+ > Na^+ > Ca^{2+} > Mg^{2+} > Pb^{2+}$). Notably, the ys-HTO@C electrode exhibits the highest Li^+ adsorption capacity (Γ (Li^+) = 7.06 mmol g^{-1}), surpassing cs-HTO@C and uncoated HTO, which present capacities of 4.75 and 4.63 mmol g^{-1}, respectively (Figs. 6b, S11b, and S12b). These data indicate that the yolk-shell architecture substantially enhances Li^+ uptake, presumably by improving electronic conductivity and providing void space for ion storage (Liu et al., 2023; Zhang et al., 2025).

In contrast, actual brine—with non-equimolar cation concentrations (Table S1)—shows that adsorption capacities for Na^+, Mg^{2+}, Ca^{2+}, and Pb^{2+} correlated positively with their respective bulk concentrations, following Γ (Na^+) > Γ (Mg^{2+}) > Γ (Ca^{2+}) > Γ (Pb^{2+}) across all HTO/carbon electrodes (Figs. 6d, S11d, and S12d). Interestingly, Li^+ adsorption dose not strictly depend on its concentration, underscoring the dominance of HTO's material-driven selectivity mechanisms over mere concentration effects (Chitrakar et al., 2014). This is further supported by their exceptionally high separation factors for Li^+ over Na^+ ($\beta_{Li/Na}$, Text S4): 60.7, 63.1, and 69.3 for ys-HTO@C, cs-HTO@C, and HTO, respectively (Figs. 6d, S11d, and S12d), in actual brine with Na^+/Li^+ molar ratio as high as 55.4 (Table S1). This high selectivity for Li^+ over Na^+ outperforms the state-of-the-art electrodes, including HTO/RGO-TA electrode ($\beta_{Li/Na}$ =56.9) (Zhang et al., 2023b), FLA-MnO_2 electrode ($\beta_{Li/Na}$ =4.37) (Bao et al., 2025), and HMO-GOH/GO electrode ($\beta_{Li/Na}$ =47.1) (Mi et al., 2025) for Li^+ extraction from Na^+-rich brines, exemplifying their superb preference of these HTO/carbon electrodes for Li^+ even under strongly competitive conditions. Notably, the pristine HTO electrode achieves the highest $\beta_{Li/Na}$, likely attributable to its minimal carbon content, which mitigates non-specific Na^+ capture (Γ (Na^+) = 20.7 mmol g^{-1} vs. 25.3 and 39.5 mmol g^{-1} for cs-HTO@C and ys-HTO@C, respectively; Figs. S11d, and S12d). Analysis of Li^+/Mg^{2+} selectivity ($\beta_{Li/Mg}$)—critical due to the physicochemical similarity between Li^+ and Mg^{2+}—reveals the same relative trend as for Na^+, confirming the inherent Li^+ ion preference endorsed by the HTO frameworks

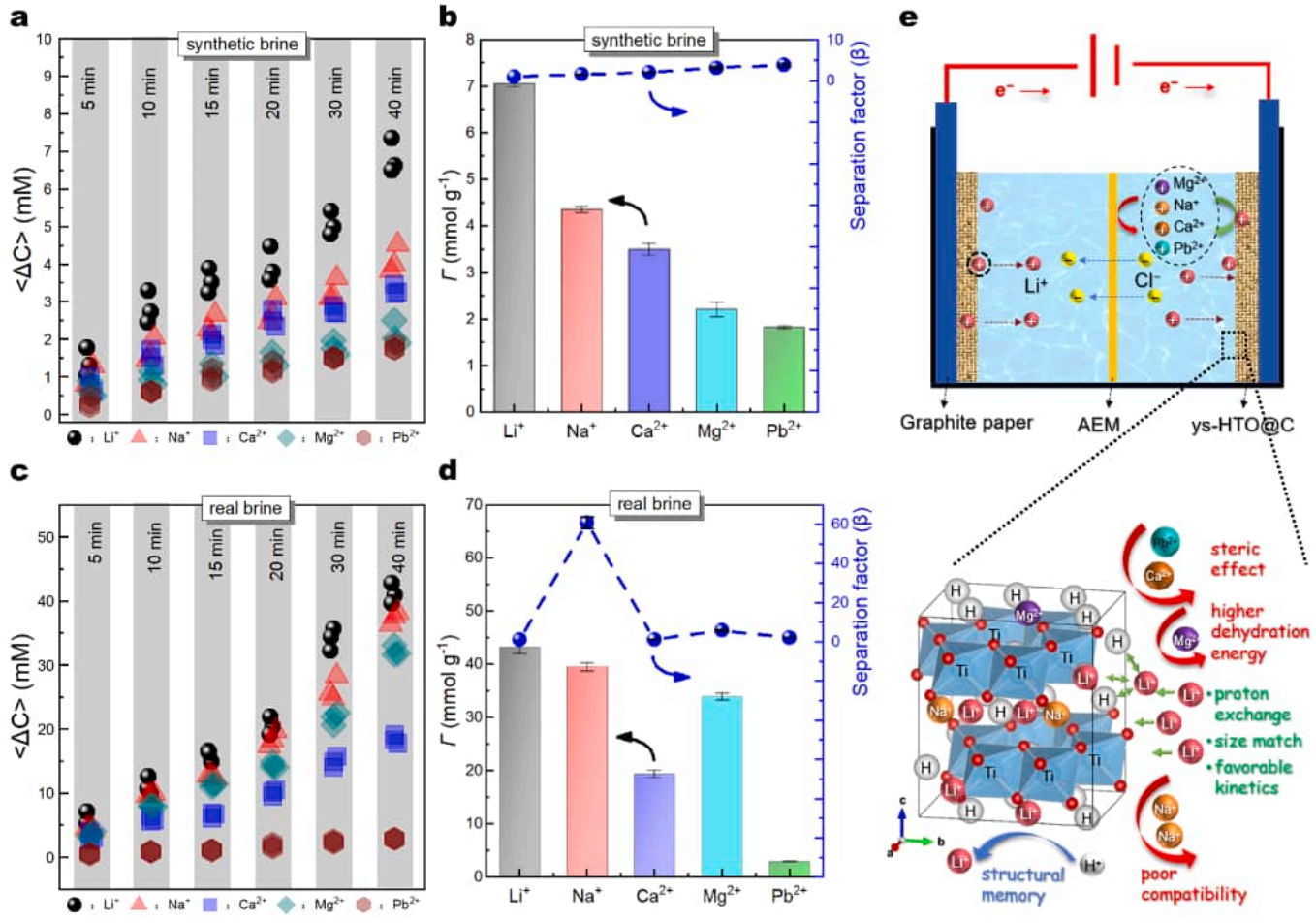

Fig. 6. Selectivity for lithium against other cations of the ys-HTO@C electrodes applied in RCDI cells: (**a**) Cation concentration variation (ΔC) over time in the synthetic brine (10 mM of Li^+, Na^+, Ca^{2+}, Mg^{2+}, Pb^{2+}); (**b**) the corresponding cation capacity (Γ, mmol g^{-1}) and separation factor (β) for Li^+; (**c**) cation concentration variation (ΔC) over time in the brine of the East Taijinaier Salt Lake (59.4 mM Li^+, 3289.8 mM Na^+, 32 mM Ca^{2+}, 269.1 mM Mg^{2+}, and 8.9 mM Pb^{2+}); (**d**) the corresponding Γ and separation factor; (**e**) the proposed mechanisms depicting the exceptional Li^+ selectivity of these HTO/carbon electrodes.

(Figs. 6c, S11c, and S12c) that has been fully demonstrated by earlier reports via either batch adsorption or density functional theory (DFT) calculations (Gu et al., 2018; Ren et al., 2025; Zhang et al., 2023a, 2023b). This intrinsic Li^+ selectivity also endows the ys-HTO@C electrodes with superior efficiency when compared to other electrodes applied in CDI for Li^+ extraction from brines (Table S4).

The exceptional Li^+ selectivity of these HTO/carbon electrodes can be rationalized from both material and ion-specific perspectives (Fig. 6e). From the ion perspective, tabulated data for hydrated radius, dehydration energy, and valency (Table S5) suggest that, among these cations, only Li^+ and Na^+ (monovalent) can physically accommodate within HTO crystal tunnels, as divalent cations are sterically excluded (e.g., Ca^{2+}, Pb^{2+}) or thermodynamically hindered (e.g., Mg^{2+} with a higher dehydration energy) (Chitrakar et al., 2014; Zhang et al., 2023b). Nevertheless, despite Na^+ having a smaller hydrated radius (3.58 Å) and lower dehydration energy than Li^+ (Table S5), all HTO/carbon electrodes still exhibit superior Li^+ selectivity (Figs. 6, S11, and S12). This counterintuitive preference arises mostly from the unique thermodynamics and kinetics associated with HTO's reversible proton–lithium exchange process ($H^+ \rightleftharpoons Li^+$) (Chitrakar et al., 2014), which is both energetically and structurally optimized for Li^+ (Lu et al., 2024). The dehydrated Li^+ ion (0.76 Å) is perfectly sized to occupy tetrahedral/distorted lattice sites in the [TiO_6] framework without imparting strain, and forms stronger, more stable bonds with lattice oxygens (high charge density), leading to more robust incorporation compared to Na^+ (Chitrakar et al., 2014; Xu et al., 2017). The exchange reaction is further facilitated by rapid H^+ mobility and favorable coordination shift pathways, allowing quick and efficient Li^+ intercalation (Chitrakar et al., 2014). Importantly, the so-called "structural memory" of HTO—where acid regeneration restores the pristine H^+ form without degrading the Li^+-optimized lattice—enables repeated cycling and selective Li^+ uptake (Chitrakar et al., 2014; Zhang et al., 2023b). In contrast, Na^+ exhibits poor compatibility: its larger ionic size induces lattice strain, weaker binding, slower diffusion, and more difficult desorption/regeneration, leading to its consistently lower uptake and mixed selectivity (Chitrakar et al., 2014; Xu et al., 2017). Recall that the unique void space inside the ys-HTO@C electrodes not only contributes significantly to the enhanced ion storage capacity but also improves the cycling performance (both for Na^+ ions), and thus probably facilitates the lithium storage and insertion as compared to the other counterpart electrodes.

In summary, the combination of material-intrinsic selectivity and ion-specific properties drives the outstanding Li^+ separation performance and Li^+ storage capacity in both synthetic and natural brines, validating HTO/carbon electrodes as promising candidates for targeted lithium recovery from Li-containing brines. This study also provides critical insights into designing high-performance Li^+ ion-selective electrodes.

4. Conclusion

In summary, material nano-scale architectonics is a promising strategy for constructing novel electrodes for highly efficient and selective ion capture from brines, allowing for control of capacity and preference by tailoring the configuration of electrodes. In this work, we explored the potential of yolk-shell construction in optimization of H_2TiO_3/carbon electrodes for highly efficient electrochemical desalination as well as selective lithium extraction via an RCDI platform. We observed that the yolk-shell structured H_2TiO_3/carbon electrode (ys-HTO@C) exhibits improved electrochemical properties, including a higher specific capacitance, faster ion diffusion rate, and lower charge-transfer resistance compared to its core-shell structured and bulk counterparts (i.e., cs-HTO@C and HTO electrodes). Electrochemical desalination tests in synthetic NaCl demonstrate that ys-HTO@C electrode shows a higher Na^+ adsorption capacity, faster SAR, higher charge efficiency, and higher capacity retention relative to the counterpart electrodes due to its unique void space inside. Structural analysis reveals that carbon oxidation and HTO degradation account for the capacity fading during the cycling operations. Lithium extractions demonstrate that Li^+ ion is preferred over Na^+, Ca^{2+}, Mg^{2+}, and Pb^{2+} ions in both the synthetic and actual brines by the HTO/carbon electrodes, and the adsorption shows a distinct concentration-dependent selectivity in actual brine. We identify that carbon content in electrodes plays a critical role in determining their Li^+ selectivity, namely, a higher fraction of carbon constituent lower selectivity, partially impairing the intrinsic preference of HTO toward Li^+. Our observations also validate that the Li^+ selectivity is driven by both the inherent preference of HTO (i.e., proton-Li^+ exchange, size match, "structural memory", and favorable kinetics) and the ion's properties (i.e., hydrated radius, dehydration energy, and valency). Future work may be needed to elucidate the mechanisms behind the enhanced performance of the yolk-shell HTO/carbon electrodes by DFT calculations and to address the capacity fading issue by modulating the carbon shell characteristics. Nevertheless, this study provides crucial insights into constructing electrodes for highly efficient desalination and selective Li^+ separation via CDI platforms.

CRediT authorship contribution statement

Shijun Miao: Writing – original draft, Investigation. **Pengcheng Yin:** Investigation. **Shu Zhang:** Writing – original draft, Investigation. **Zijie Zhang:** Investigation. **Dawei Li:** Supervision, Resources. **Feihu Li:** Writing – review & editing, Writing – original draft, Visualization, Supervision, Investigation, Funding acquisition, Conceptualization.

Declaration of competing interest

The authors declare that they have no known competing financial interests or personal relationships that could have appeared to influence the work reported in this paper.

Acknowledgments

The authors are grateful to Dr. Jun Li and Dr. Mingzhe Dong at the Qinghai Institute of Salt Lakes, Chinese Academy of Sciences (CAS), for providing the East Taijinaier Salt Lake brine.

Supplementary materials

Supplementary material associated with this article can be found, in the online version, at doi:10.1016/j.watres.2025.124785.

Data availability

Data will be made available on request.

References

Aramesh, M., Tran, P.A., Ostrikov, K., Prawer, S., 2017. Conformal nanocarbon coating of alumina nanocrystals for biosensing and bioimaging. Carbon 122, 422–427.
Bandina, E., Elkabous, M., Iurchenkova, A., El Ouardi, Y., Repo, E., 2025. 3D-printed polyamide-H_2TiO_3 composite for selective lithium adsorption: insights from experimental and theoretical dynamic simulations studies. Miner. Eng. 231, 109470.
Bao, Y., Hao, J.X., Zhang, S., Zhu, D.C., Li, F.H., 2023. Structural/compositional-tailoring of nickel hexacyanoferrate electrodes for highly efficient capacitive deionization. Small 19 (34), 2300384.
Bao, Y., Jin, J., Ma, M.Y., Li, M., Li, F.H., 2022. Ion exchange conversion of Na-birnessite to Mg-buserite for enhanced and preferential Cu^{2+} removal via hybrid capacitive deionization. ACS Appl. Mater. Interfaces 14 (41), 46646–46656.
Bao, Y., Ling, Y.J., Ji, Z.Y., Zhou, H.R., Song, S.X., Jia, F.F., Li, J.B., Quintana, M., 2025. Lithium extraction from low-grade brines via strain-induced electronic structure modulation of MnO_2 nanorods through Mg incorporation. J. Mater. Chem. A 13 (28), 22470–22482.
Brezesinski, T., Wang, J., Tolbert, S.H., Dunn, B., 2010. Ordered mesoporous α-MoO_3 with iso-oriented nanocrystalline walls for thin-film pseudocapacitors. Nat. Mater. 9 (2), 146–151.
Chitrakar, R., Makita, Y., Ooi, K., Sonoda, A., 2014. Lithium recovery from salt lake brine by H_2TiO_3. Dalton Trans. 43 (23), 8933–8939.

Elimelech, M., Phillip, W.A., 2011. The future of seawater desalination: energy, technology, and the environment. Science 333 (6043), 712–717.
Gamaethiralalage, J.G., Singh, K., Sahin, S., Yoon, J., Elimelech, M., Suss, M.E., Liang, P., Biesheuvel, P.M., Zornitta, R.L., de Smet, L.C.P.M., 2021. Recent advances in ion selectivity with capacitive deionization. Energy Environ. Sci. 14 (3), 1095–1120.
Gan, Y.M., Liu, L.Z., Zhang, Q.X., Huang, J.N., Han, S.J., Chen, B.B., Liu, Y., Yu, Q.M., Guan, L.H., Zhou, T.H., Han, M., Zhao, Y., Huang, W., 2023. Internal interface engineering of yolk-shell structure toward fast and robust potassium storage. Energy Storage Mater. 59, 102794.
Gao, X., Omosebi, A., Landon, J., Liu, K.L., 2015. Surface charge enhanced carbon electrodes for stable and efficient capacitive deionization using inverted adsorption-desorption behavior. Energy Environ. Sci. 8 (3), 897–909.
Gu, D.L., Sun, W.J., Han, G.F., Cui, Q., Wang, H.Y., 2018. Lithium ion sieve synthesized via an improved solid state method and adsorption performance for West Taijinar Salt Lake brine. Chem. Eng. J. 350, 474–483.
Guo, Z.X., Shen, G.Z., Wang, Z.P., Ma, Q.H., Zhang, L.Y., Xiao, B., Yan, Y.D., Zheng, Y.L., Liu, Y., Yuan, X., 2024. Integrating FeOOH with bacterial cellulose-derived 3D carbon nanofiber aerogels for fast and stable capacitive deionization based on accelerating chloride insertion. Desalination 576, 117329.
Hagemans, F., Vlug, W., Raffaelli, C., van Blaaderen, A., Imhof, A., 2017. Sculpting silica colloids by etching particles with nonuniform compositions. Chem. Mater. 29 (7), 3304–3313.
Han, L.C., Karthikeyan, K.G., Anderson, M.A., Wouters, J.J., Gregory, K.B., 2013. Mechanistic insights into the use of oxide nanoparticles coated asymmetric electrodes for capacitive deionization. Electrochim. Acta 90, 573–581.
Jin, J., Bao, Y., Li, F.H., 2025. Enhanced removal of Cu and Pb ions from wastewater via a hybrid capacitive deionization platform with MnO_2/N-doped mesoporous carbon nanocomposite electrodes. ACS Appl. Mater. Interfaces 17 (9), 13783–13793.
Jin, J., Li, M., Tang, M.T., Li, Y., Liu, Y.Y., Cao, H., Li, F.H., 2020. Phase- and crystallinity-tailorable MnO_2 as an electrode for highly efficient hybrid capacitive deionization (HCDI). ACS Sustain. Chem. Eng. 8 (30), 11424–11434.
Kong, L.C., Yan, G.B., Hu, K.J., Yu, Y.C., Conte, N., Mckenzie Jr., K., Wagner, M.J., Boyes, S.G., Chen, H.N., Liu, C., Liu, X.T., 2025. Electro-driven direct lithium extraction from geothermal brines to generate battery-grade lithium hydroxide. Nat. Commun. 16, 806.
Li, J.R., Tang, Z.L., Zhang, Z.T., 2005. Layered hydrogen titanate nanowires with novel lithium intercalation properties. Chem. Mater. 17 (23), 5848–5855.
Li, J.R., Tang, Z.L., Zhang, Z.T., 2006. Pseudocapacitive characteristic of lithium ion storage in hydrogen titanate nanotubes. Chem. Phys. Lett. 418 (4–6), 506–510.
Li, Y., Yang, Z., Ma, P.H., 2023. Research progress on new types of H_2TiO_3 lithium-ion sieves: a review. Metals 13 (5), 977.
Liu, X.H., Xu, X.T., Xuan, X.X., Xia, W., Feng, G.L., Zhang, S.H., Wu, Z.G., Zhong, B.H., Guo, X.D., Xie, K.Y., Yamauchi, Y., 2023. Unlocking enhanced capacitive deionization of $NaTi_2(PO_4)_3$/carbon materials by the yolk-shell design. J. Am. Chem. Soc. 145 (16), 9242–9253.
Liu, Y., Wang, L.H., Ma, Q.H., Xu, X.T., Gao, X., Zhu, H.G., Feng, T., Dou, X.Y., Eguchi, M., Yamauchi, Y., Yuan, X., 2024. Simultaneous generation of residue-free reactive oxygen species and bacteria capture for efficient electrochemical water disinfection. Nat. Commun. 15, 10175.
Liu, Y.J., Wang, W.Q., Chen, Q.D., Xu, C., Cai, D.P., Zhan, H.B., 2019. Resorcinol formaldehyde resin-coated prussian blue core shell spheres and their derived unique yolk shell FeS_2@C spheres for lithium-ion batteries. Inorg. Chem. 58 (2), 1330–1338.
Lu, M.X., Miao, Y., Yang, Y., Li, P., 2024. DFT calculation and experiments for Li^+/H^+ ion-exchange on titanium-based lithium ion-sieves. Chem. Eng. Sci. 300, 120619.
Ma, Q.H., Wang, Z.P., Zhang, L.Y., Xiao, B., Zhang, L., Xiao, C.Y., Zhang, W.Y., Xia, J.H., Liu, Y., Yuan, X., 2025. Marrying Fe nanoclusters with 3D carbon nanofiber aerogels: triggering fast and robust faradic capacitive deionization. Sep. Purif. Technol. 353, 128503.
Marthi, R., Asgar, H., Gadikota, G., Smith, Y.R., 2021. On the structure and lithium adsorption mechanism of layered H_2TiO_3. ACS Appl. Mater. Interfaces 13 (7), 8361–8369.
Mi, A., Qin, X.B., Zhang, F., Yun, R.P., Zhao, Y.J., Wang, M., Xiang, X., 2025. Enhanced lithium extraction from high-sodium brines: modification of a manganese-based ion sieve using hydroxylated graphene and graphene oxide. Desalination 604, 118694.
Mousset, E., Fournier, M., Su, X., 2023. Recent advances of reactive electroseparation systems for water treatment and selective resource recovery. Curr. Opin. Electrochem. 42, 101384.
Oren, Y., 2008. Capacitive deionization (CDI) for desalination and water treatment - past, present and future (a review). Desalination 228 (1–3), 10–29.
Orooji, Y., Nezafat, Z., Nasrollahzadeh, M., Shafiei, N., Afsari, M., Pakzad, K., Razmjou, A., 2022. Recent advances in nanomaterial development for lithium ion-sieving technologies. Desalination 529, 115624.
Porada, S., Weinstein, L., Dash, R., van der Wal, A., Bryjak, M., Gogotsi, Y., Biesheuvel, P. M., 2012. Water desalination using capacitive deionization with microporous carbon electrodes. ACS Appl. Mater. Interfaces 4 (3), 1194–1199.
Porada, S., Zhao, R., van der Wal, A., Presser, V., Biesheuvel, P.M., 2013. Review on the science and technology of water desalination by capacitive deionization. Prog. Mater. Sci. 58 (8), 1388–1442.
Ren, Y.C., Zhao, D.D., Zhou, F., Fu, C., Fu, Y.S., Wu, Z.L., Luo, Y., Sun, F., He, X., Sun, X. P., 2025. self-assemblied HTO/MXene/PSF hybrid membrane for high efficiency and selective lithium extraction from shale gas wastewater. Nano Res. 18 (4), 94907261.
Seo, H.Y., Choi, J.H., Kim, Y.B., Cho, J.S., Kang, Y.C., Park, G.D., 2023. Tailoring the shell thickness of yolk-shell structured carbon microspheres: applications in metal selenide and carbon composite microspheres for enhanced sodium ion storage properties. J. Mater. Chem. A 11 (45), 24738–24753.
Shang, X.H., Liu, J.Y., Hu, B., Nie, P.F., Yang, J.M., Zhang, B.S., Wang, Y.W., Zhan, F., Qiu, J.S., 2022. CNT-strung $LiMn_2O_4$ for lithium extraction with high selectivity and stability. Small Methods 6 (7), 2200508.
Smith, B.C., 2022. Infrared spectroscopy of polymers, IX: pendant ester polymers and polycarbonates. Spectroscopy 37 (11), 16–19.
Srimuk, P., Su, X., Yoon, J., Aurbach, D., Presser, V., 2020. Charge-transfer materials for electrochemical water desalination, ion separation and the recovery of elements. Nat. Rev. Mater. 5 (7), 517–538.
Srimuk, P., Zeiger, M., Jackel, N., Tolosa, A., Kruner, B., Fleischmann, S., Grobelsek, I., Aslan, M., Shvartsev, B., Suss, M.E., Presser, V., 2017. Enhanced performance stability of carbon/titania hybrid electrodes during capacitive deionization of oxygen saturated saline water. Electrochim. Acta 224, 314–328.
Sun, J., Li, X.W., Huang, Y.H., Luo, G.L., Tao, D.J., Yu, J.T., Chen, L.L., Chao, Y.H., Zhu, W.S., 2023. Preparation of high hydrophilic H_2TiO_3 ion sieve for lithium recovery from liquid lithium resources. Chem. Eng. J. 453, 139485.
Sun, K.G., Tebyetekerwa, M., Zeng, X.K., Wang, Z.Y., Duignan, T.T., Zhang, X.W., 2024. Understanding the electrochemical extraction of lithium from ultradilute solutions. Environ. Sci. Technol. 58 (8), 3997–4007.
Suss, M.E., Porada, S., Sun, X., Biesheuvel, P.M., Yoon, J., Presser, V., 2015. Water desalination via capacitive deionization: what is it and what can we expect from it? Energy Environ. Sci. 8 (8), 2296–2319.
Tian, C.X., Ma, G.Q., Ge, H.W., 2023. Structural evolution of metatitanic acid and iron removal during hydrolysis of industrial $TiOSO_4$ solution. Sci. Rep. 13, 8509.
Wang, H., Shi, L.Y., Yan, T.T., Zhang, J.P., Zhong, Q.D., Zhang, D.S., 2014. Design of graphene-coated hollow mesoporous carbon spheres as high performance electrodes for capacitive deionization. J. Mater. Chem. A 2 (13), 4739–4750.
Wang, J., Polleux, J., Lim, J., Dunn, B., 2007. Pseudocapacitive contributions to electrochemical energy storage in TiO2(anatase) nanoparticles. J. Phys. Chem. C 111 (40), 14925–14931.
Wang, S.L., Zhang, M., Zhang, Y., Zhang, Y., Qiao, S., Zheng, S.L., 2019a. Application of citric acid as eluting medium for titanium type lithium ion sieve. Hydrometallurgy 183, 166–174.
Wang, S.Y., Wang, G., Wu, T.T., Li, C.P., Wang, Y.W., Pan, X., Zhan, F., Zhang, Y.Q., Wang, S.F., Qiu, J.S., 2019b. Membrane-free hybrid capacitive deionization system based on redox reaction for high-efficiency NaCl removal. Environ. Sci. Technol. 53 (11), 6292–6301.
Wei, S.D., Wei, Y.F., Chen, T., Liu, C.B., Tang, Y.H., 2020. Porous lithium ion sieves nanofibers: general synthesis strategy and highly selective recovery of lithium from brine water. Chem. Eng. J. 379, 122407.
Xu, X., Chen, Y.M., Wan, P.Y., Gasem, K., Wang, K.Y., He, T., Adidharma, H., Fan, M.H., 2016. Extraction of lithium with functionalized lithium ion-sieves. Prog. Mater. Sci. 84, 276–313.
Xu, X., Zhou, Y., Fan, M.H., Lv, Z.J., Tang, Y., Sun, Y.Z., Chen, Y.M., Wan, P.Y., 2017. Lithium adsorption performance of a three-dimensional porous H_2TiO_3-type lithium ion-sieve in strong alkaline Bayer liquor. RSC Adv. 7 (31), 18883–18891.
Xu, Y.S., Chen, B.J., Jiang, T., Zhou, H.J., 2025. Rational in-situ construction of oxygen-deficient and carbon-coated TiO_2 hollow nanotubes for high-performance electrochemical desalination. Chem. Eng. J. 521, 166487.
Yang, S.X., Wang, Y.G., Pan, H., He, P., Zhou, H.S., 2024. Lithium extraction from low-quality brines. Nature 636 (8042), 309–321.
Yu, H.W., Wang, C., Phuntsho, S., He, T., Naidu, G., Han, D.S., Shon, H.K., 2025. Highly selective lithium recovery from seawater desalination brine using Li_2TiO_3 membrane-coated capacitive deionization. Water Res 285, 124113.
Zhai, H.F., Xia, B.Y., Park, H.S., 2019. Ti-based electrode materials for electrochemical sodium ion storage and removal. J. Mater. Chem. A 7 (39), 22163–22188.
Zhang, C.Y., Yao, J.R., Zhai, W.T., Chen, H., He, H.L., Zhang, Y.B., He, T., 2023a. Lithium extraction from geothermal brine by granulated HTO titanium-based adsorbent with block-co-polymer poly (ethylene-co-vinyl alcohol) (EVAL) as binder. Chem. Eng. J. 467, 143526.
Zhang, J.X., Cheng, Z.Y., Qin, X.B., Gao, X., Yun, R.P., Xiang, X., 2023b. Bifunctional modification enhances lithium extraction from brine using a titanium-based ion sieve membrane electrode. ACS Appl. Mater. Interfaces 15 (24), 29586–29596.
Zhang, S., Ye, Z.N., Ma, M.Y., Yin, P.C., Bao, Y., Li, F.H., 2025. Optimizing the integration of nickel hexacyanoferrate with hollow mesoporous carbon spheres (HMCSs) for highly efficient capacitive deionization. Desalination 603, 118679.
Zhou, J.G., Xu, Y.S., Shin, D.M., Zhou, H.J., 2025. Breaking the trade-off between capacity, stability, and selectivity for electrochemical lithium extraction via a dual-ion doping strategy. Desalination 600, 118530.